Dependency of the impacts of geoengineering on the stratospheric sulfur injection strategy – Part 2: How changes in the hydrological cycle depend on injection rates and model?

Anton Laakso[1], Daniele Visioni[2], Ulrike Niemeier[3], Simone Tilmes[4], and Harri Kokkola[1]

[1]Finnish Meteorological Institute, Atmospheric Research Centre of Eastern Finland, Kuopio, 70200, Finland
[2]Department of Earth and Atmospheric Sciences, Cornell University, Ithaca, NY 14850, USA
[3]Max Planck Institute for Meteorology, Bundesstr. 53, 20146 Hamburg, Germany
[4]National Center for Atmospheric Research, Boulder, CO 80307, USA

Correspondence: Anton Laakso (anton.laakso@fmi.fi)

Abstract. This is the second of two papers where we study the dependency of the impacts of stratospheric sulfur injections on the used model and injection strategy. Here, aerosol optical properties from simulated stratospheric aerosol injections using two aerosol models (modal scheme M7 and sectional scheme SALSA), as described in Part 1, are implemented consistently into EC-Earth, MPI-ESM and CESM Earth System Models to simulate the climate impacts of different injection rates ranging from

5 2 to 100 $Tg(S)yr^{-1}$. Two sets of simulations were simulated with the three ESMs: 1) Regression simulations, where abrupt change in CO_2 concentration or stratospheric aerosols over preindustrial conditions were applied to quantify global mean fast temperature independent climate responses and quasi-linear dependence on temperature and 2) equilibrium simulations, where radiative forcing of aerosol injections with various magnitudes compensate the corresponding radiative forcing of CO_2 enhancement to study the dependence of precipitation on the injection magnitude; the latter also allow to explore the regional

10 climatic responses. Large differences in SALSA and M7 simulated radiative forcings in Part 1 translated into large differences in the estimated surface temperature and precipitation changes in ESM simulations: e.g. an injection rate of 20 $Tg(S)yr^{-1}$ in CESM using M7 simulated aerosols led to only 2.2 K global mean cooling while EC-Earth - SALSA combination produced 5.2 K change. In equilibrium simulations, where aerosol injections were utilized to offset the radiative forcing caused by an atmospheric CO_2 concentration of 500 ppm, the decrease in global mean precipitation varied among models, ranging from

15 -0.7% to -2.4% compared to the preindustrial climate. These precipitation changes can be explained by the fast precipitation response due to radiation changes caused by the stratospheric aerosols and CO_2 because global mean fast precipitation response is shown to be negatively correlated with global mean atmospheric absorption. Our study shows that estimating the impact of stratospheric aerosol injection on climate is not straightforward. This is because the capability of the sulfate layer to reflect solar radiation and absorb LW radiation is sensitive to the injection rate as well as the aerosol model used to simulate the

20 aerosol field. These findings emphasize the necessity for precise simulation of aerosol microphysics to accurately estimate the climate impacts of stratospheric sulfur intervention. This study also reveals gaps in our understanding and uncertainties that still exist related to these controversial techniques.

atmosphere. The impact of LW absorption becomes stronger if larger injection rates are applied. This is also linked to how aerosols are modelled: in Part 1 SW radiative forcing was 45%–85% higher and LW radiative forcing was 24%-40% lower in simulations with SALSA than in M7. This indicates that there would be significant differences in the simulated climate

60   responses depending on how the aerosols are simulated. The situation is further complicated by the lack of clear criteria for selecting the appropriate aerosol model. Observations following the 1991 Pinatubo eruption have frequently been utilized as a benchmark for evaluating models' ability to simulate stratospheric aerosols. However, a single sulfur injection, as in the case of Pinatubo, differs significantly from continuous injections in case of SAI. Notably, there is a minimal difference between the M7 and SALSA model results in the simulations of the Pinatubo eruption, as detailed in (Kokkola et al., 2018). Simulations

65   using the M7 model were 60% faster than those with SALSA, but there were some numerical limitations associated with the modes in M7, which restricted the aerosols from achieving an optimal size range for effectively scattering radiation, as noted in Laakso et al. (2022). However, the performance of the M7 results is also sensitive to the configuration of the modes, making it difficult to predict which setup will perform well, as the performance depends on the simulated case (i.e volcanic eruption vs. SAI, different injection strategies for SAI).

70   Changes in atmospheric radiation have a direct impact also on precipitation. Precipitation changes can be explained by the changes the total column atmospheric energy budget (O'Gorman et al., 2012). The atmosphere possesses a relatively low heat capacity, and following a perturbation, it rapidly reaches a state where the incoming and outgoing energy fluxes to and from the atmosphere balance each other. In other words, the budget of perturbations between two atmospheric states can be expressed as:

75   $L\delta P = \delta R_{Surf} - \delta R_{TOA} + \delta SH = -\delta R_{abs} + \delta SH,$ (1)

where L is the latent heat of condensation, P is precipitation, R_{TOA} and R_{Surf} are the change in the radiative fluxes at the top of the atmosphere and surface, SH is the sensible heat flux change and δR_{abs} is the change in absorbed radiation. Niemeier et al. (2013), showed that changes in global latent heat flux dominate changes in sensible heat flux, establishing a roughly linear relationship between precipitation and the discrepancy between the radiative imbalance at the surface and at the

80   top of the atmosphere. Other studies have also shown that changes in precipitation are proportional to the difference between changes in radiation at the surface and in the atmosphere, i.e absorbed radiation (O'Gorman et al., 2012; Kravitz et al., 2013b; Liepert and Previdi, 2009). The atmospheric energy budget can also be utilized to represent precipitation in a transient climate. Given that radiation (and changes in atmospheric absorption) are known to be relatively linearly correlated with global mean precipitation, as evidenced by climate models (e.g (Zelinka et al., 2020)) and observations (Koll and Cronin, 2018) precipitation

85   change can be approximated by a simple equation comprising temperature-dependent and independent components(s):

$\delta P = a\delta T + F = P_{slow} + P_{fast},$ (2)

where δT is global mean temperature change, a is constant and F are the temperature independent components. Within this equation, $a\delta T$ accounts for all feedbacks attributable to temperature change, including the variation in surface sensible heat flux. This is often referred to as the slow precipitation response or component, which changes over a multi-year timescale

same injection profile by making injections continuously to the equator only, and ignore changes in strategy using spatial and temporal variation, as done in Part 1.

2 Models and Simulations

2.1 Models

2.1.1 Earth System Models: EC-Earth, MPI-ESM and CESM

We used three state-of-the-art Earth System Models (ESM), which all include modules for the atmosphere, land and ocean. These models are Max Planck Institute Earth System Model (MPI-ESM1.2) (Mauritsen et al., 2019), Community Earth System Model (CESM2.1.2) (Danabasoglu et al., 2020) and EC-Earth (3.3.1, Döscher et al. (2022)). These models represent a wide range of climate sensitivities (effective climate sensitivity in CO_2 quadrupling experiment: MPI-ESM: 3.13 K, EC-Earth: 4.1 K, CESM: 5.15 K) present in CMIP6 models (Zelinka et al., 2020). MPI-ESM consists of the atmospheric models ECHAM6.3, Max Planck Institute Ocean Model (MPIOM) (includes the HAMOCC ocean biogeochemistry model) and the JSBACH land model. CESM 2.0 consists of the Community Atmospheric Model (CAM6),Parallel Ocean Program (POP2) ocean model, the Community Land Model (CLM4), and Community Ice CodE (CICE4) sea ice model. For EC-Earth, atmospheric, ocean, land and ocean biochemistry models are: IFS, NEMO, LPJ-GUESS and PISCES, respectively. Thus these three ESMs do not share the same model components and the results can be considered relatively independent of each other. However radiative transfer module in all three ESMs (and in the aerosol-climate model used to simulate aerosol optical properties of aerosols fields in Part 1) are based on rapid radiative transfer model which uses the 14 SW and 16 LW radiation bands (Döscher et al., 2022; Danabasoglu et al., 2020; Mauritsen et al., 2019). This makes implementation of optical properties of stratospheric aerosols rather straightforward. The resolution of atmosphere used in MPI-ESM, CESM and EC-Earth simulations are T63L47 (1.9° x 1.9°), finite volume 0.9°x1.25° and 32 vertical levels and T255L91 (0.70° x 0.70°) respectively.

2.1.2 Aerosol-Climate model ECHAM-HAMMOZ used in Part 1

Simulations in Part 1 were done with the aerosol climate model ECHAM-HAMMOZ (ECHAM6.3-HAM2.3-MOZ1.0) (Zhang et al., 2012; Kokkola et al., 2018; Schultz et al., 2018; Tegen et al., 2019). The atmospheric model is the same as in the MPI-ESM version used in this study (Stevens et al., 2013). Simulations were performed with a T63L95 (i.e. 1.9°x1.9°) resolution, which enables resolving the quasi-biennial oscillation (QBO). Aerosols were simulated by two different aerosol modules: the sectional module SALSA, where aerosols are represented by 10 size bins in size space, and the modal module M7, which has 4 modes in size space. 7 years (roughly 3 whole QBO cycles) simulations were done for each scenario. A more detailed description of the model is found in (Laakso et al., 2022).
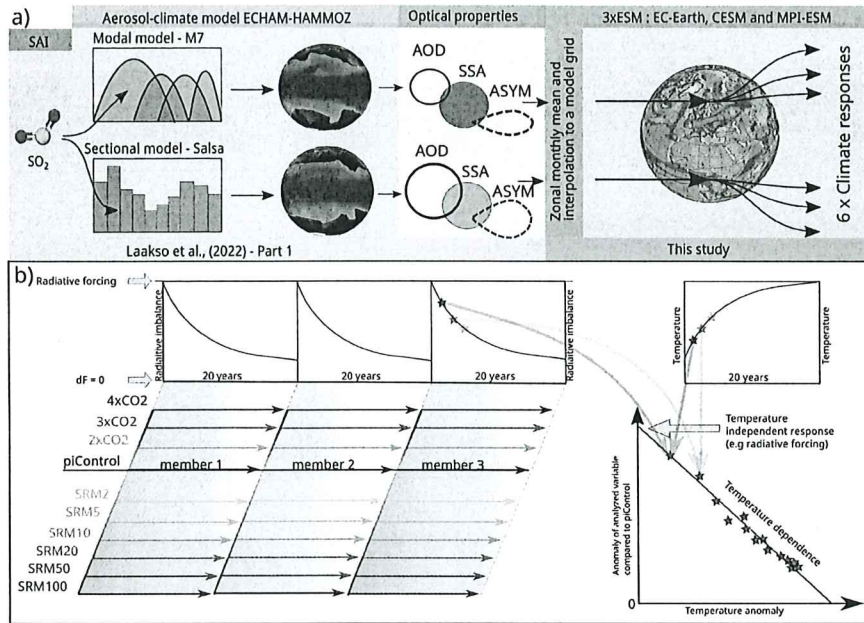
5

Figure 1. a) A schematic of the implementation of aerosol optical properties simulated in (Laakso et al., 2022) to ESMs in this study. b) Simulated regression scenarios and using them to quantify global mean temperature independent responses and quasi-linear dependence on global mean temperature.

a band across all longitudes between the latitudes 10° N and 10° S. The injection was done vertically at 20-22 km altitude. Simulations were done for yearly injection rates of 1, 2, 5, 10, 20, 50, 100 Tg(S)yr^{-1}. ~~However, here~~ we excluded the 1 Tg(S)yr^{-1} simulation as we wanted to concentrate on climatically-relevant, and more signal-to-noise scenarios, to analyse climate impacts in extreme conditions. Simulations were performed with both SALSA and M7 aerosol modules.

2.4.2 Regression simulations

The regression simulations with ESMs were started from a preindustrial baseline with GHG and SAI perturbations applied. For SAI, these perturbations were stratospheric aerosol fields (from simulations with 2, 5, 10, 20, 50, 100 Tg(S)yr^{-1} injection rates) from SALSA and M7 produced in Part 1. In addition, regression simulations with $2xCO_2$, $3xCO_2$ and $4xCO_2$ abrupt forcings were done as well as one simulation in preindustrial conditions without any perturbation. As Richardson et al. (2016) pointed out, a regression length less than 15 years might lead to variation in the quantified fast and feedback responses. On the other hand a longer regression would improve statistics, but then long-scale feedbacks would have a larger role which would lead to a slight nonlinearity. ~~Here~~ we chose 20 years as the regression length, and to improve the statistics, we simulated three ensemble members.
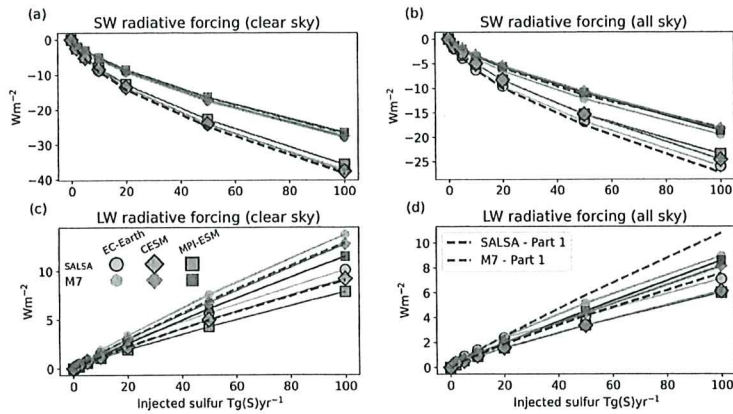
7

Figure 2. Global mean short-wave a) clear sky and b) all-sky and global mean long-wave c) clear sky and d) all-sky radiative forcing as a function of injection rate. Solid lines are radiative forcing from ESM simulations with SALSA and M7 simulated aerosols and based on regression simulations. Dashed lines shows results from Laakso et al. (2022).

3 Summary of Part 1 and evaluating the implementation of stratospheric sulfur aerosol fields in ESMs

In Part 1, stratospheric sulfur injections were simulated with a sectional aerosol module SALSA and a modal aerosol module M7. Simulated radiative forcings are shown in Fig. 2. Simulations with both models showed that the SW radiative forcing increased sub-linearly with the injection rate while the increase in LW forcing was more linear. In other respects, there was a significant difference between the model results: SW all-sky radiative forcing was 45-85% higher when based on SALSA simulations than with M7 whereas LW radiative forcing was 32-67% higher in M7 than in SALSA depending on the injection rate. Thus, the total radiative forcing was 88% - 154% higher in SALSA than in M7. Details behind these differences are discussed in Laakso et al. (2022), but generally M7 produced significantly larger aerosols than SALSA. This was caused by both the treatment of the modal size distribution in M7, which prevented aerosols from having an optimal size for scattering under continuous injections, and that in SALSA injected sulfur tended to form new particles instead of condensating on the existing ones, while M7 displayed the opposite behavior.

To ensure that implementation of stratospheric aerosols is done correctly the radiative forcing simulated by each ESMs is compared to the radiative forcing simulated by ECHAM-HAMMOZ in Part 1 (Fig. 2). When comparing these results to the radiative forcings in Part 1, it should be kept in mind that the method for quantifying radiative forcings was different for ESM simulations compared to Part 1, which makes them slightly different measures. Radiative forcing of SAI scenarios in ESM is calculated based on Gregory plots for all-sky SW, LW and total radiative forcings of regression simulations (Gregory et al., 2004). These plots are shown in the Supplement Fig. S1-3. As figures show, global mean radiation flux changes are rather linear compared to global temperature change. From these figures we can quantify radiative forcings from the y-intercept. In Part 1, radiative forcing was calculated by double radiation call with and without aerosols from simulations with fixed sea

9

started (considering a fixed amount injected per year). This measure is called effective climate sensitivity (the term is generally used for, specifically, the corresponding temperature change for 2xCO$_2$ experiment). It does not take into account some of the longer-term nonlinear climate feedbacks that are accounted for in the equilibrium climate sensitivity. Nevertheless, the effective climate sensitivity is a good estimate of temperature changes without simulations spanning over thousands of years,

260 which would be required to quantify equilibrium climate sensitivity (Gregory et al., 2004). However, it should be kept in mind that temperature change estimates at equilibrium are underestimated if quantified from the effective climate sensitivity; this is especially true here, where we define the slope only from the first 20 years after the induced forcing.

In addition to the magnitude of radiative forcing, the temperature change is influenced by feedback mechanisms, which vary in magnitude for each of the ESM. Some of the simulated scenarios were quite extreme and led to over six degrees change in

265 global mean temperature already during our 20-year simulation period. This naturally has a large impact on feedbacks, especially the ones that are not always linearly dependent on temperature e.g., cloud and albedo feedbacks. Thus, the dependence of radiative flux chance on global mean temperature is not totally linear.

Figure 3a shows the global mean temperature change as a function of the injection rate of SAI in MPI-ESM, CESM and EC-Earth based on effective climate sensitivity. As the figure shows, simulations where SALSA modelled aerosols are implemented

270 lead to significantly larger global mean cooling compared to M7 aerosols. As expected, larger radiative forcings from SALSA-simulated aerosols translate to a larger global mean temperature change. In addition, based on M7, cooling impact decreases much faster as a function of injection rate than if aerosols are simulated with SALSA, which is also the same pattern in which we saw global mean radiative forcings (Fig. 2). There also are differences in the results between ESMs. Cooling is largest in EC-Earth compared to other ESMs with the same aerosols. In EC-Earth both the total radiative forcing and effective

275 climate sensitivity parameter were slightly larger (more negative) compared to the other models. Overall, the variation in results between the ESMs was smaller compared to the difference originating from using different aerosol microphysics (M7 vs. SALSA).

In Fig. 3a CESM shows the lowest temperature change in SAI simulations even though based on 4xCO$_2$ simulation in (Zelinka et al., 2020), the CESM climate sensitivity was higher compared to EC-Earth and MPI-ESM. This is partly explained

280 by different responses to the SAI and change in CO$_2$ concentration: In CESM, the climate sensitivity parameter (i.e., the slope of the TOA radiative forcing as a function of temperature change) seems to be lower under CO$_2$ induced warming than when negative radiative forcing was induced with SAI (see Supplement Fig. S3). This means that CO$_2$ induced forcing causes larger temperature change than corresponding forcing induced by SAI. However, based on 4xCO$_2$ simulations in this study, the effective climate sensitivities are 7.97 K, 7.80 K and 5.66 K for EC-Earth, CESM and MPI-ESM respectively, while

285 corresponding values were 8.2 K, 10.3 K and 5.96 K (MPI-ESM-HR) in Zelinka et al. (2020). Note that values reported in Zelinka et al. (2020) are x-intercept values from the Gregory plots divided by 2. In this study, effective climate sensitivity was defined based on the first 20 years after induced forcing, whereas Zelinka et al. (2020) quantified it from 150 years. In Supplement Fig. S4 we used Coupled Model Intercomparison Project 6 data from 4xCO$_2$ experiment of EC-Earth, CESM and MPI-ESM and showed how the slope of the radiation vs. temperature change regression line depends on the number of years

290 used to make the fit and to calculate the climate sensitivity. As this figure shows, the slope becomes smaller and the effective

11

So these values are for 4x CO2 at equilibrium, right? (based on the equilibrium intercept)

What climate sensitivity to drastically different for 2xCO2. Isn't it misleading?

cancellation of LW radiative forcing from CO_2. Similarly, as for radiative forcing, the fast precipitation change can be defined from regression simulations by regressing precipitation against the global mean temperature (see Supplement Fig. S6). Fast precipitation change is then given by the y-intercept. Fig. 3b shows the fast precipitation response in each simulation as function of injection rate. For some simulations with small injection rates, the response is small compared to the error bars (shaded area in the figure). In general, the fast precipitation response is more positive in simulations where SALSA aerosols are used compared to ones with M7 aerosols in corresponding ESM simulations and the differences between aerosol models become more pronounced with higher injection rates. These differences among aerosol model results are even more apparent when the fast precipitation response is presented as a function of radiative forcing. For SALSA aerosols, a lower injection rate can achieve the same level of radiative forcing as M7, resulting in more significant differences in fast precipitation responses (see supplement figure Fig. S7a). In addition, the fast precipitation response is non-linear as a function of both injection rate and radiative forcing. However, the standard deviation of the simulated fast precipitation response between model combinations is rather linear with respect to the injection rate and the simulated radiative forcing. (see Supplement Fig. S8). This means that the differences in the simulated fast precipitation response between models become larger with larger injections.

In simulations with SALSA aerosols in EC-Earth and CESM, the fast precipitation is positive for all simulated injection rates except for 100 Tg(S)yr^{-1} in EC-Earth. With M7 aerosol in EC-Earth and CESM, the fast precipitation response is slightly positive or small if 20 Tg(S)yr^{-1} or less is injected but negative with 50 or 100 Tg(S)yr^{-1} injection rates. Results in MPI-ESM differ from CESM and EC-Earth results. In MPI-ESM, the fast precipitation response is small (<0.13% of the global mean precipitation) with SALSA aerosols with lower than 20 Tg(S)yr^{-1} injection rate. However for larger injection rates the fast precipitation response was -0.6% and -1.83% lower than the global mean precipitation in piControl simulation. Fast precipitation response in MPI-ESM-M7 simulations was also much more negative than CESM-M7 and EC-Earth-M7 simulations. Overall quantified fast precipitation response due to the SAI varied between 0.69% increase in global mean precipitation to -3.19% reduction in precipitation depending on injection rate and ESM-aerosol model combination. Based on the average hydrological sensitivity in our simulations (Supplement Fig. S6), which were 2.46 %K^{-1} (σ=0.28 %K^{-1}) the range between the maximum and minimum fast precipitation responses corresponds to a global mean precipitation change associated with a temperature variation of 1.6 K.

Fast precipitation changes as a function of injection rate can be understood based on the absorbed radiation. As forcing (change in CO_2 concentration or added aerosols) is induced, it changes the radiation absorbed by the atmosphere. E.g. in the case of higher CO_2 concentration, more LW radiation is absorbed. Aerosols also absorb LW radiation, but as aerosols in the stratosphere reflect solar radiation back to space, there is less radiation to be absorbed by the background atmosphere under the SAI aerosol layer. Figure 4a shows the net absorption immediately after when forcing is induced (i.e. absorption part of radiative forcing) versus fast precipitation responses in each simulated scenario. As figure shows, fast precipitation response and change in absorbed radiation are fairly linearly dependent as shown also by Samset et al. (2016) and Laakso et al. (2020). This relation was quantified for each model separately even though there are not large differences between models. We can use this quantity to calculate the individual contribution of SW and LW radiation change to fast precipitation change. This is shown by dashed and dot-dashed lines in Fig. 4 b,c,d for individual ESM and by using M7 and SALSA aerosols. As less SW
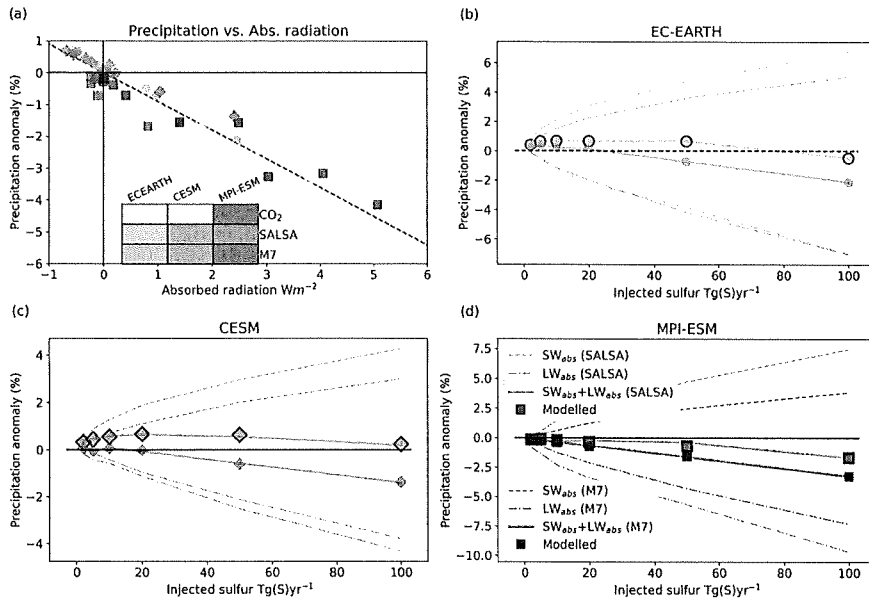
Figure 4. a) Regression of fast precipitation response versus atmospheric absorption, b-d) precipitation anomaly as a function of injection rate in EC-Earth, CESM and MPI-ESM respectively. Markers are quantified from regression simulations by regressing precipitation against temperature while lines are calculated from atmospheric absorption based on the relation in a). The dashed line is precipitation change caused by SW absorption, the dash-dotted line is based on LW absorption and the solid line is the sum of these SW and LW components whereas markers are modelled fast precipitation responses from regression simulations.
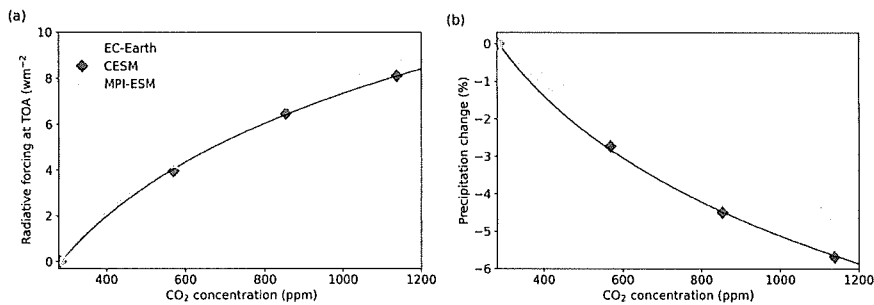

Figure 5. a) Radiative forcing at the top of the atmosphere and b) fast precipitation response as a function of atmospheric CO_2 concentration based on logarithmical fit for results from piControl, $2xCO_2$, $3xCO_2$ and $4xCO_2$ scenarios

by CO_2 depends logarithmically on the atmospheric concentration of CO_2, we used a logarithmic fit to determine the radiative forcing for each of the four simulated values (see Fig. 5). This function provides the radiative forcing for a particular CO_2

385 concentration for each of the three ESMs. By utilizing this function and the radiative forcings for each SAI simulation, we can
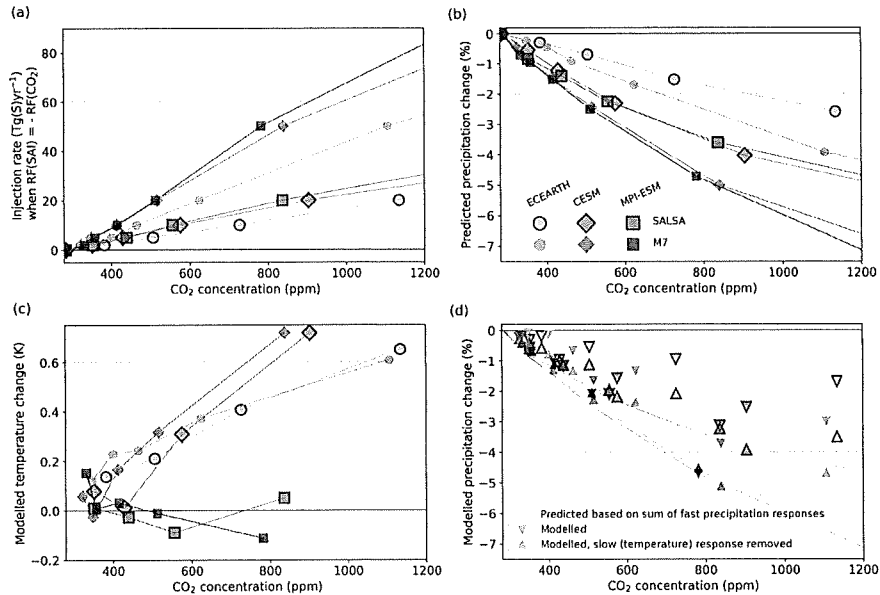
15

Figure 6. a) The estimated injection rate of stratospheric sulfur injections and b) estimated precipitation change in different model combinations if radiative forcing (RF) of CO_2 concentration is compensated by SAI. Global mean precipitation change is calculated as the sum of the fast precipitation changes from SAI and CO_2, assuming that there is no change in global mean temperature. Based on the logarithmic relationship between radiative forcing and fast precipitation response to CO_2 concentration (as shown in Fig. 5), the CO2 concentration and the subsequent fast precipitation response can be determined from the logarithmic fit so that the radiative forcing aligns with the simulated radiative forcing for SAI. c) Simulated changes in a) global mean temperature and b) precipitation under SAI - CO_2 pair scenarios (as illustrated in a), assuming a state of climate equilibrium. In d) "triangle down"-marker shows actual simulated precipitation, "triangle up"-marker shows adjusted values based on hydrological sensitivity and assuming zero global mean temperature change and solid line shows estimated precipitation change based on fast precipitation changes (same as in b)).

across various simulated forcing agents. Simulations using CESM and MPI-ESM suggest that the hydrological sensitivity increases with larger injections, but the range of this increase differs significantly from the sensitivity observed in simulations where CO_2 concentration was perturbed. Conversely, in EC-EARTH simulations, hydrological sensitivity ranged from 2.39 to 2.48 $\%K^{-1}$ in scenarios with CO_2 perturbations, while in SAI scenarios, the total range was 2.79 - 3.22 $\%K^{-1}$. This discrepancy is a crucial factor to consider, especially in cases where the forcing induced by CO_2 and SAI does not fully offset each other but might also have an impact when those are expected to compensate each other.

4.2 Results of climate equilibrium simulations

Next, we conducted simulations where radiative forcing from CO_2 and SAI compensated each other based on the SAI experiment-atmospheric CO_2 concentration pairs calculated in the previous section. These simulations allowed us to observe how well our estimations for precipitation changes (Fig. 6b) held and, additionally, to simulate regional changes. The simu-

17

4.2.2 Simulated global mean precipitation change in climate equilibrium simulations

465 As there is an increase in global mean temperature in these simulations, the actual simulated global mean precipitation differs fundamentally from the estimated ones in the previous section. In Fig. 6d, the solid lines show the estimated precipitation change using fast precipitation responses (same as Fig. 6b). Triangle markers that point down show the actual simulated precipitation in these scenarios. As global mean temperature changes were rather small in the MPI-ESM simulations, the actual simulated precipitation changes were close to the estimated ones. However, as there was a slight warming in the EC-Earth and 470 CESM simulations, global mean precipitation is more positive than those estimated from the sum of fast precipitation responses. Hydrological sensitivity (i.e., the ratio of precipitation change to temperature change) can be used to remove the impact of global mean temperature on precipitation. Triangle markers that point up are adjusted values of simulated precipitation by counteracting the impact of temperature change. Now, the adjusted values from CESM simulations are close to the estimated ones. For EC-Earth, this adjustement corrects precipitation values to the direction of estimated ones, but it over-adjusts them 475 for most of the simulated scenarios. It remains unclear why this temperature adjustment leads to an overestimation in the results for EC-Earth simulations. However, this could be related to the larger hydrological sensitivities for SAI compared to CO_2 perturbations, as discussed in section 4.1.3. Although there are discrepancies between the actual simulated values and the estimated ones, this analysis shows that estimating the total precipitation change based on the sum of fast precipitation responses of SAI and change in CO_2 concentration gives rather good results even though there are some changes in global 480 mean temperature. The main conclusions also hold after analyzing the actual simulations: there are large variations in global mean precipitation between models, and larger aerosols based on M7 lead to a larger reduction in precipitation than those simulated by SALSA.

4.2.3 Regional temperature responses in the equilibrium scenarios

Figure 7 shows the zonal mean, and Fig. 8 the regional temperature response in the climate equilibrium simulations for selected 485 scenarios. The regional responses for all scenarios are shown in supplementary Fig. S10-11. Several earlier studies have shown that compensating GHG-induced warming with low-latitude SAI or SRM generally leads to residual warming in high latitudes and overcooling at low latitudes(e.g., Schmidt et al. (2012); Kravitz et al. (2013a); Visioni et al. (2021)), unless the injections are explicitly targeted to avoid this imbalance ((Kravitz et al., 2017, 2019; MacMartin et al., 2017)). Laakso et al. (2022) demonstrated that the radiative forcing from SAI is primarily concentrated around the Equator for aerosols simulated using 490 both SALSA and M7 models. There was also significant clear-sky zonal forcing observed at the latitudes of 50°N and 50°S. However, the presence of clouds in these regions reduced the aerosol all-sky radiative forcing. Aerosol optical properties were consistently applied across all three ESMs, but variations in cloud cover and properties among the ESMs can lead to differences in the actual radiative impact of aerosols.

Here overcooling of tropics is seen only in MPI-ESM simulations. As there was global mean warming in the CESM and EC-495 Earth simulations, there are fewer and smaller regions compared to the MPI-ESM simulations that show negative temperature anomaly, especially within scenarios with larger atmospheric CO_2 concentrations and SAI. However, in simulations using these
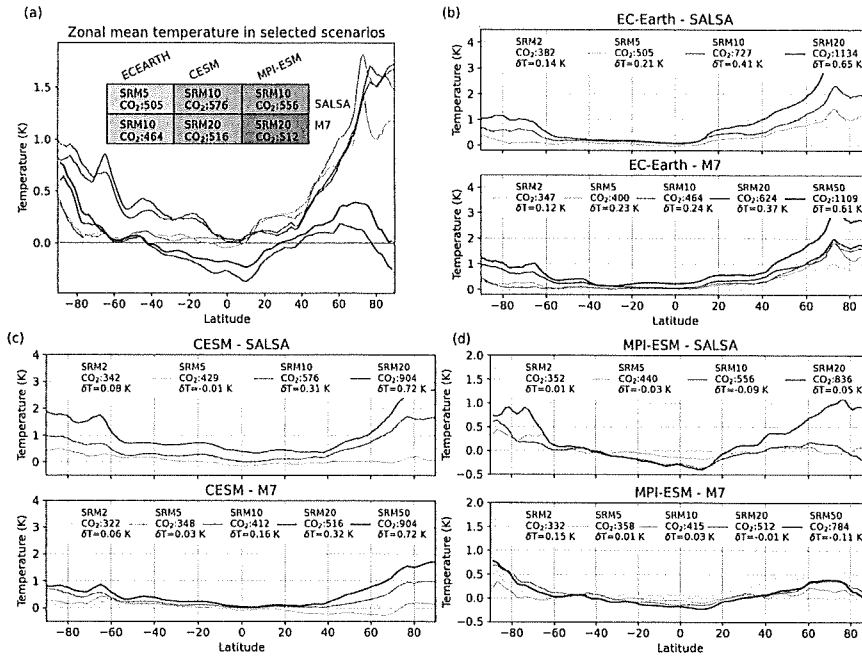
19

Figure 7. Zonal mean temperature (a) for climate equilibrium scenarios where atmospheric CO_2 concentration was between 464-576 ppm and climate equilibrium scenarios for (b) EC-Earth, (c) CESM, and (d) MPI-ESM. In these simulations, the CO_2 concentration was adjusted to counterbalance the radiative forcing from a specific injection rate, as determined by regression simulations. δT in the legends shows residual global mean temperature.

Atlantic Meridional Overturning Circulation seen also in simulations with global warming (Meehl et al., 2020; Fasullo and Richter, 2023).

4.2.4 Regional precipitation responses in the equilibrium scenarios

Figure 9 shows differences in zonal mean precipitation and Fig. 10 shows the regional precipitation difference between climate
535 equilibrium simulation and piControl as an average of 30 years. In earlier sections, we focused on yearly mean values or mean periods over several years. Therefore, in this section, we focus only on averages over the years and do not analyze seasonal impacts. The regional precipitation change patterns show a shift of Intertropical Convergence Zone (ITCZ) and a reduction of precipitation over land, but as for the temperature impacts, the changes intensify when the CO_2 concentration in the atmosphere and the injection rate of SAI increase. Statistical significant precipitation changes are observed only in
540 a minority of regions, particularly in weaker-forcing cases with low CO_2 increase and SAI injection rates. Similar to the temperature changes discussed in the previous section, there are no significant differences in regional patterns of precipitation change between using M7 or SALSA aerosols. However, larger CO_2 concentration and larger forcing from SAI when SALSA aerosols are used lead to a more intensive impact than the corresponding injection rate using M7 aerosols.
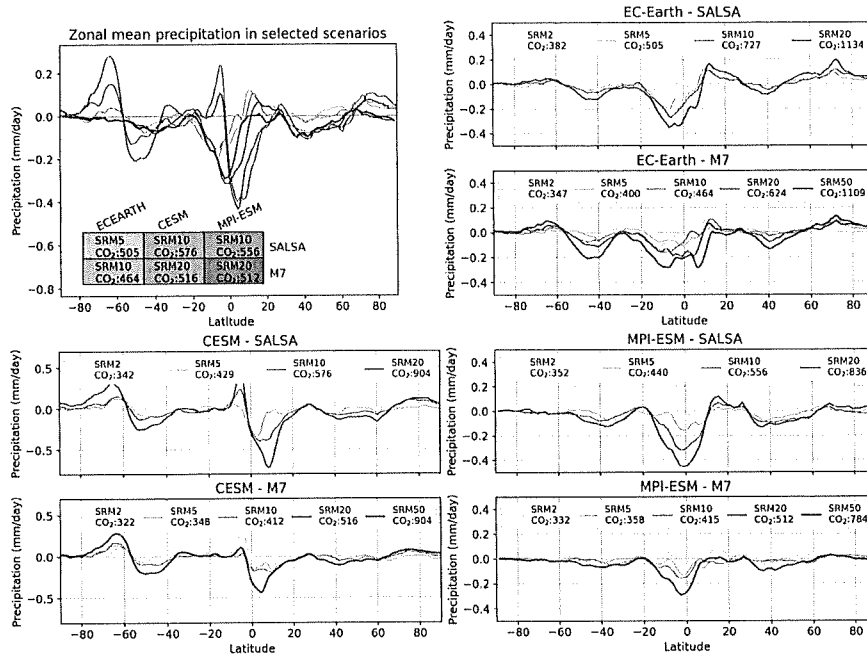
Figure 9. Zonal mean precipitation (a) for climate equilibrium scenarios where atmospheric CO_2 concentration were between 464-576 ppm and climate equilibrium scenarios for (b) EC-Earth, (c) CESM and (d) MPI-ESM.

that region. CESM results indicate a strong intensification of precipitation over the Equator, which is not observed in EC-Earth and MPI-ESM results. On the other hand, there are also regions where model results agree with each other. Generally, precipitation decreases over oceans (except for the Equator in CESM results). Precipitation increases over Australia, as well as in the

555 Arabian Peninsula, Pakistan, and India, but decreases over the northern parts of South America.

5   Conclusions and discussion

In Laakso et al. (2022), we simulated SAI of different magnitudes using the sectional (SALSA) and modal (M7) aerosol schemes, which showed significant differences in the simulated radiative forcings between the two aerosol models. In this study, we implemented the simulated radiative properties into three ESMs (EC-Earth, CESM, and MPI-ESM) to study the

560 temperature and precipitation responses under different magnitudes of SAI, based on the results from the two aerosol schemes. This was done through two sets of simulations, using the aerosol optical properties from the preceding SALSA and M7 simulations for injection rates of 2-100 $Tg(S)yr^{-1}$: 1) regression simulations were conducted under preindustrial conditions with the additional instantaneous forcing, and 2) alleged climate equilibrium simulations were performed, where the global mean radiative forcings of CO_2 increase and SAI compensated each other.

23

our regression simulations for 20 $Tg(S)yr^{-1}$ injection rate, the projected range for global mean temperature change spanned between -2.2 K and -5.2 K. Further, this range can be subdivided into two groups: -(2.2 - 2.8 K) for ESM simulations where M7 aerosols were used, and -(4.0 - 5.2 K) for simulations based on SALSA. Simulated temperature change was smallest in CESM simulations based on both SALSA and M7 aerosols despite that climate sensitivity of CESM has been shown to be markedly higher compared to other two ESMs (Zelinka et al., 2020). This discrepancy was attributed to determining the climate sensitivity parameter based on a 20-year span rather than a 150-year period, as e.g., in Zelinka et al. (2020), but also differences in responses to the SW vs. LW radiative forcing or cooling vs. warming. Except for most extreme impact simulated in this study (simulating 100 $Tg(S)^{-1}$ injection rate with SALSA), the temperature change was largest in EC-Earth simulations. This resulted from both a slightly larger climate sensitivity parameter (based on a 20-year span) and a larger simulated radiative forcing of SAI in EC-Earth compared to the other two ESMs. Overall, drawing from these results and a comparison with the climate sensitivities reported in (Zelinka et al., 2020), it should be kept in mind that effective climate sensitivity is not a straightforward parameter. Its interpretation is complicated by its sensitivity to external factors, such as the type of forcing agent (which affects shortwave vs. longwave radiation) and the length of the simulation period (e.g., 20 years vs. 100 years). Moreover, sensitivity to these external factors varies across different models..

Based on the radiative forcings quantified from regression simulations we estimated the annual sulfur injection required to compensate for the radiative forcing of CO_2 ranging from preindustrial concentration to 1200ppm (see section 4.1.3). The results varied significantly among different combinations of ESM-aerosol models. By making interpolation between simulated results, offsetting the radiative forcing from 500 ppm atmospheric CO_2 concentrations, required sulfur injection rate varied between 5-19 $Tg(S)yr^{-1}$ between aerosol-ESM model combinations. As expected, the most significant differences arose from the choice of aerosol model used for simulations. Estimates for the required injection rate varied from 5 to 8 $Tg(S)yr^{-1}$ when SALSA aerosols were employed, and from 12 to 19 $Tg(S)yr^{-1}$ with M7-simulated aerosols. By using quantified fast precipitation responses, we were able to estimate subsequent changes in global mean precipitation under these scenarios, assuming no alteration in global mean temperature due to the presumed climate equilibrium. This led to a reduction in precipitation across all simulated scenarios. In the aforementioned 500ppm atmospheric CO_2 concentration and SAI scenario the resulting reduction compared to preindustrial climate in global mean precipitation ranged from 0.7% to 2.4% between different model combinations (Fig. 6). In the same CO_2 concentration within the same ESM, a larger decrease in precipitation was consistently observed when M7 aerosols were used compared to SALSA aerosols. However, when considering different ESMs, there was no distinct separation between SALSA aerosol-based simulations, which exhibited a global mean precipitation reduction ranging from 0.7% to 1.8%, and M7-based simulations, which showed a reduction ranging from 1.4% to 2.4%." When conducting the actual simulations for these presumed climate equilibrium scenarios, we observed that the assumption of no change in global mean temperature was valid only for the MPI-ESM simulation. In contrast, in the CESM and EC-Earth simulations, there was global mean warming of up to 0.7 K in certain runs. Hence, the range for simulated precipitation reduction in the presumed climate equilibrium scenario for 500 ppm was 0.5% to 2.0%, which was slightly different from the earlier estimate.

We looked deeper into global precipitation impacts caused directly by SAI analyzing its fast precipitation response. There were large differences between fast precipitation responses between model combinations: the CESM-SALSA combination

of the background atmosphere and surface, such as clouds, albedo, aerosols, and gaseous components. Model features and simulation characteristics, like resolution, interpolation of SAI fields, differences in radiation schemes, or how these schemes are integrated with the atmospheric model, might also play a role. An in-depth analysis of these factors is beyond the scope of this study. In equilibrium simulations (see Fig. 6), variations in precipitation responses across the ESMs are influenced also by disparities in the fast precipitation response to CO_2 and the radiative forcing of CO_2 (Fig. 5). In these simulations, the radiative forcing of CO_2 also determines the SAI injection rate, which varies for each model (Fig. 6a)

The findings presented in this study, as well as Part 1, illustrate that variations arising from the microphysical scale and the modeling of microphysical processes can result in substantial discrepancies in the global-scale climate impacts of SAI. This highlights the significant uncertainty that microphysics introduces into our estimations of SAI impacts. Therefore, greater effort should be made to improve the representation of microphysical processes in stratospheric conditions and to understand the observed differences in results between aerosol climate models (Quaglia et al., 2023).

The analysis presented here was largely based on the quasi-linear assumption of a relationship between near-surface temperature and radiation or global mean precipitation change in the case of an abrupt change in the forcing agent. As it is generally known and demonstrated here, this assumption does not completely hold, especially for simulations spanning decades. Even though the method is not perfect, the analysis was consistent across all models used here and proved to be a useful tool in analyzing the factors behind simulated responses.

This study only covers continuous equatorial injection within the longitude bands examined in Laakso et al. (2022) (referred to as the baseline scenario). In Laakso et al. (2022), we simulated various alternative injection strategies involving different magnitudes, and temporal and spatial injection patterns. Many of these alternative scenarios were found to be more effective strategies to scatter SW radiation and absorb less LW radiation than the baseline scenario used in this study. For instance, in the seasonal injection scenario examined in Laakso et al. (2022), which involved seasonal changes to the injection area, the simulated SW radiative forcing at an injection rate of 20 $Tg(S)yr^{-1}$ with M7 was 30% greater than in the injection scenario examined here. However, the difference in LW radiative forcing was small between the two injection scenarios. If similar climate equilibrium simulations, as we did here with baseline injection strategy, were done with seasonal injection strategy, a smaller injection rate would be required. Simultaneously less LW radiation would be absorbed and thus it would result smaller reduction in global mean precipitation than we saw in Fig. 6. Seasonal injection strategy also would probably lead to a more equal compensation of temperature change across latitudes and lesser warming in the Arctic region in climate equilibrium-style simulations since the forcing would be more concentrated in mid-latitudes than the tropics compared to equatorial injections. Simulating different injection strategies with ESMs is a subject for future research.

The overall results of this study indicate that there are significant uncertainties regarding the estimated impacts of the possible deployment of SAI (e.g the coefficient of variation of the fast precipitation response below injection rate 50 $Tg(S)yr^{-1}$ was above 1.5). There are large discrepancies in global mean responses of radiative forcings, temperature, and precipitation, as well as the required amount of sulfur to achieve a certain target, depending on the aerosol and Earth System Model used. These quantities are essential for any consideration related to solar radiation management, and the large uncertainties regarding them raise concerns about the more uncertain quantities, such as regional responses or extreme climate impacts under SAI.

27

References

Bjordal, J., Storelvmo, T., Alterskjær, K., and Carlsen, T.: Equilibrium climate sensitivity above 5 °C plausible due to state-dependent cloud feedback, Nature Geoscience, 13, 718–721, https://doi.org/10.1038/s41561-020-00649-1, 2020.

Danabasoglu, G., Lamarque, J.-F., Bacmeister, J., Bailey, D. A., DuVivier, A. K., Edwards, J., Emmons, L. K., Fasullo, J., Garcia, R., 690 Gettelman, A., Hannay, C., Holland, M. M., Large, W. G., Lauritzen, P. H., Lawrence, D. M., Lenaerts, J. T. M., Lindsay, K., Lipscomb, W. H., Mills, M. J., Neale, R., Oleson, K. W., Otto-Bliesner, B., Phillips, A. S., Sacks, W., Tilmes, S., van Kampenhout, L., Vertenstein, M., Bertini, A., Dennis, J., Deser, C., Fischer, C., Fox-Kemper, B., Kay, J. E., Kinnison, D., Kushner, P. J., Larson, V. E., Long, M. C., Mickelson, S., Moore, J. K., Nienhouse, E., Polvani, L., Rasch, P. J., and Strand, W. G.: The Community Earth System Model Version 2 (CESM2), Journal of Advances in Modeling Earth Systems, 12, e2019MS001 916, https://doi.org/https://doi.org/10.1029/2019MS001916, 695 e2019MS001916 2019MS001916, 2020.

Döscher, R., Acosta, M., Alessandri, A., Anthoni, P., Arsouze, T., Bergman, T., Bernardello, R., Boussetta, S., Caron, L.-P., Carver, G., Castrillo, M., Catalano, F., Cvijanovic, I., Davini, P., Dekker, E., Doblas-Reyes, F. J., Docquier, D., Echevarria, P., Fladrich, U., Fuentes-Franco, R., Gröger, M., v. Hardenberg, J., Hieronymus, J., Karami, M. P., Keskinen, J.-P., Koenigk, T., Makkonen, R., Massonnet, F., Ménégoz, M., Miller, P. A., Moreno-Chamarro, E., Nieradzik, L., van Noije, T., Nolan, P., O'Donnell, D., Ollinaho, P., van den Oord, 700 G., Ortega, P., Prims, O. T., Ramos, A., Reerink, T., Rousset, C., Ruprich-Robert, Y., Le Sager, P., Schmith, T., Schrödner, R., Serva, F., Sicardi, V., Sloth Madsen, M., Smith, B., Tian, T., Tourigny, E., Uotila, P., Vancoppenolle, M., Wang, S., Wårlind, D., Willén, U., Wyser, K., Yang, S., Yepes-Arbós, X., and Zhang, Q.: The EC-Earth3 Earth system model for the Coupled Model Intercomparison Project 6, Geoscientific Model Development, 15, 2973–3020, https://doi.org/10.5194/gmd-15-2973-2022, 2022.

Fasullo, J. T. and Richter, J. H.: Dependence of strategic solar climate intervention on background scenario and model physics, Atmospheric 705 Chemistry and Physics, 23, 163–182, https://doi.org/10.5194/acp-23-163-2023, 2023.

Ferraro, A. J., Highwood, E. J., and Charlton-Perez, A. J.: Weakened tropical circulation and reduced precipitation in response to geoengineering, Environmental Research Letters, 9, 014 001, https://doi.org/10.1088/1748-9326/9/1/014001, 2014.

Gregory, J. M., Ingram, W. J., Palmer, M. A., Jones, G. S., Stott, P. A., Thorpe, R. B., Lowe, J. A., Johns, T. C., and Williams, K. D.: A new method for diagnosing radiative forcing and climate sensitivity, Geophysical Research Letters, 31, 710 https://doi.org/https://doi.org/10.1029/2003GL018747, 2004.

Heckendorn, P., Weisenstein, D., Fueglistaler, S., Luo, B. P., Rozanov, E., Schraner, M., Thomason, L. W., and Peter, T.: The impact of geoengineering aerosols on stratospheric temperature and ozone, Environmental Research Letters, 4, 045 108, https://doi.org/10.1088/1748-9326/4/4/045108, 2009.

Kokkola, H., Kühn, T., Laakso, A., Bergman, T., Lehtinen, K. E. J., Mielonen, T., Arola, A., Stadtler, S., Korhonen, H., Ferrachat, S., 715 Lohmann, U., Neubauer, D., Tegen, I., Siegenthaler-Le Drian, C., Schultz, M. G., Bey, I., Stier, P., Daskalakis, N., Heald, C. L., and Romakkaniemi, S.: SALSA2.0: The sectional aerosol module of the aerosol–chemistry–climate model ECHAM6.3.0-HAM2.3-MOZ1.0, Geoscientific Model Development, 11, 3833–3863, https://doi.org/10.5194/gmd-11-3833-2018, 2018.

Koll, D. D. B. and Cronin, T. W.: Earth's outgoing longwave radiation linear due to H_2O greenhouse effect, Proceedings of the National Academy of Sciences, 115, 10 293–10 298, https://doi.org/10.1073/pnas.1809868115, 2018.

720 Kravitz, B., Caldeira, K., Boucher, O., Robock, A., Rasch, P. J., Alterskjær, K., Karam, D. B., Cole, J. N. S., Curry, C. L., Haywood, J. M., Irvine, P. J., Ji, D., Jones, A., Kristjánsson, J. E., Lunt, D. J., Moore, J. C., Niemeier, U., Schmidt, H., Schulz, M., Singh, B., Tilmes, S.,

29

Myhre, G., Forster, P. M., Samset, B. H., Hodnebrog, O., Sillmann, J., Aalbergsjø, S. G., Andrews, T., Boucher, O., Faluvegi, G., Fläschner,
760   D., Iversen, T., Kasoar, M., Kharin, V., Kirkevåg, A., Lamarque, J.-F., Olivié, D., Richardson, T. B., Shindell, D., Shine, K. P., Stjern, C. W.,
        Takemura, T., Voulgarakis, A., and Zwiers, F.: PDRMIP: A Precipitation Driver and Response Model Intercomparison Project—Protocol
        and Preliminary Results, Bulletin of the American Meteorological Society, 98, 1185 – 1198, https://doi.org/10.1175/BAMS-D-16-0019.1,
        2017.

        Niemeier, U. and Timmreck, C.: What is the limit of climate engineering by stratospheric injection of SO_2?, Atmospheric Chemistry and
765   Physics, 15, 9129–9141, https://doi.org/10.5194/acp-15-9129-2015, 2015.

        Niemeier, U., Schmidt, H., and Timmreck, C.: The dependency of geoengineered sulfate aerosol on the emission strategy, Atmospheric
        Science Letters, 12, 189–194, https://doi.org/10.1002/asl.304, 2011.

        Niemeier, U., Schmidt, H., Alterskjær, K., and Kristjánsson, J. E.: Solar irradiance reduction via climate engineering: Impact of differ-
        ent techniques on the energy balance and the hydrological cycle, Journal of Geophysical Research: Atmospheres, 118, 11,905–11,917,
770   https://doi.org/https://doi.org/10.1002/2013JD020445, 2013.

        O'Gorman, P. A., Allan, R. P., Byrne, M. P., and Previdi, M.: Energetic Constraints on Precipitation Under Climate Change, Surveys in
        Geophysics, 33, 585–608, https://doi.org/10.1007/s10712-011-9159-6, 2012.

        Pierce, J. R., Weisenstein, D. K., Heckendorn, P., Peter, T., and Keith, D. W.: Efficient formation of stratospheric aerosol for climate engi-
        neering by emission of condensible vapor from aircraft, Geophysical Research Letters, 37, https://doi.org/10.1029/2010GL043975, 2010.

775   Quaglia, I., Timmreck, C., Niemeier, U., Visioni, D., Pitari, G., Brodowsky, C., Brühl, C., Dhomse, S. S., Franke, H., Laakso, A., Mann,
        G. W., Rozanov, E., and Sukhodolov, T.: Interactive stratospheric aerosol models' response to different amounts and altitudes of SO_2
        injection during the 1991 Pinatubo eruption, Atmospheric Chemistry and Physics, 23, 921–948, https://doi.org/10.5194/acp-23-921-2023,
        2023.

        Richardson, T. B., Samset, B. H., Andrews, T., Myhre, G., and Forster, P. M.: An assessment of precipitation ad-
780   justment and feedback computation methods, Journal of Geophysical Research: Atmospheres, 121, 11,608–11,619,
        https://doi.org/https://doi.org/10.1002/2016JD025625, 2016.

        Russotto, R. D. and Ackerman, T. P.: Changes in clouds and thermodynamics under solar geoengineering and implications for required solar
        reduction, Atmospheric Chemistry and Physics, 18, 11 905–11 925, https://doi.org/10.5194/acp-18-11905-2018, 2018.

        Samset, B. H., Myhre, G., Forster, P. M., Hodnebrog, O., Andrews, T., Faluvegi, G., Fläschner, D., Kasoar, M., Kharin, V., Kirkevåg,
785   A., Lamarque, J.-F., Olivié, D., Richardson, T., Shindell, D., Shine, K. P., Takemura, T., and Voulgarakis, A.: Fast and slow pre-
        cipitation responses to individual climate forcers: A PDRMIP multimodel study, Geophysical Research Letters, 43, 2782–2791,
        https://doi.org/https://doi.org/10.1002/2016GL068064, 2016.

        Schmidt, H., Alterskjær, K., Bou Karam, D., Boucher, O., Jones, A., Kristjánsson, J. E., Niemeier, U., Schulz, M., Aaheim, A., Benduhn, F.,
        Lawrence, M., and Timmreck, C.: Solar irradiance reduction to counteract radiative forcing from a quadrupling of CO_2: climate responses
790   simulated by four earth system models, Earth System Dynamics, 3, 63–78, https://doi.org/10.5194/esd-3-63-2012, 2012.

        Schultz, M. G., Stadtler, S., Schröder, S., Taraborrelli, D., Franco, B., Krefting, J., Henrot, A., Ferrachat, S., Lohmann, U., Neubauer,
        D., Siegenthaler-Le Drian, C., Wahl, S., Kokkola, H., Kühn, T., Rast, S., Schmidt, H., Stier, P., Kinnison, D., Tyndall, G. S., Orlando,
        J. J., and Wespes, C.: The chemistry–climate model ECHAM6.3-HAM2.3-MOZ1.0, Geoscientific Model Development, 11, 1695–1723,
        https://doi.org/10.5194/gmd-11-1695-2018, 2018.

795   Seeley, J. T., Lutsko, N. J., and Keith, D. W.: Designing a Radiative Antidote to CO2, Geophysical Research Letters, 48, e2020GL090 876,
        https://doi.org/https://doi.org/10.1029/2020GL090876, e2020GL090876 2020GL090876, 2021.